# Radar Image Study of Simulated Breaking Waves

Hyunjun Kim, *Student Member, IEEE,* and Joel T. Johnson, *Member, IEEE*

***Abstract*—Radar images of electromagnetic scattering from one-dimensional simulated ocean breaking waves are described. Backscatter results from 10–14 GHz at 60° to 80° incident angles are considered for surfaces that satisfy an impedance boundary condition. The generalized forward–backward method with spectral accelerations was used as an exact numerical solution to obtain backscatter returns from several surface profiles, and radar images are formed through back-projection tomography. Detailed investigations of the images are provided to clarify major and secondary scattering events, as well as the polarization dependence, and a ray-tracing analysis is performed to interpret multipath scattering mechanisms. By adding surface roughness outside the breaking region, small-scale roughness scattering effects are also investigated.**

***Index Terms*—Breaking waves, generalized forward–backward method, multipath scattering, radar imaging.**

## I. Introduction

SEA SURFACE scattering is of particular interest in microwave remote sensing. Several experiments and numerical simulations of laboratory breaking waves have been performed to suggest that the breaking portion of an ocean surface plays an important role in "superevent" or "sea-spike" scattering phenomena [1]–[4], where horizontal–horizontal/vertical–vertical cross-section ratios become unity or larger. Strong multiple interactions between breaking points and other surface points have been proposed to explain observed scattering behaviors at near-grazing incidence angles [5], [6]. Although numerical scattering calculations with breaking-wave profiles can reproduce many of the observed effects, obtaining insight into the surface features that produce particular radar returns can be difficult from numerical data alone.

Imaging techniques can provide a means for analysis and better understanding of rough-surface scattering phenomena in various situations [7]–[9]. Recent development of efficient numerical methods for backscattering predictions has enabled radar image formation with simulated data [10], [11]. Previous radar image studies based on a power-law surface model (Pierson–Moskowitz spectrum) have shown some multiple interaction effects due to the Bragg scattering component in conjunction with the longwave portion of the surface [12]. Though the Pierson–Moskowitz surface model produces important image features such as polarization dependencies, surface tilting effects, and surface roughness length scale effects, the power-law surface model is unable to explain the "superevent" phenomenon. This motivates extension of radar image studies to more realistic cases involving breaking-wave models.

Manuscript received October 18, 2001; revised April 16, 2002.

H. Kim is with Intel Corporation, Chandler, AZ 85226 USA (e-mail: hyunjun.kim@intel.com).

J. T. Johnson is with the ElectroScience Laboratory, Department of Electrical Engineering, The Ohio State University, Columbus, OH 43212 USA (e-mail: johnson@ee.eng.ohio-state.edu).

Digital Object Identifier 10.1109/TGRS.2002.802475

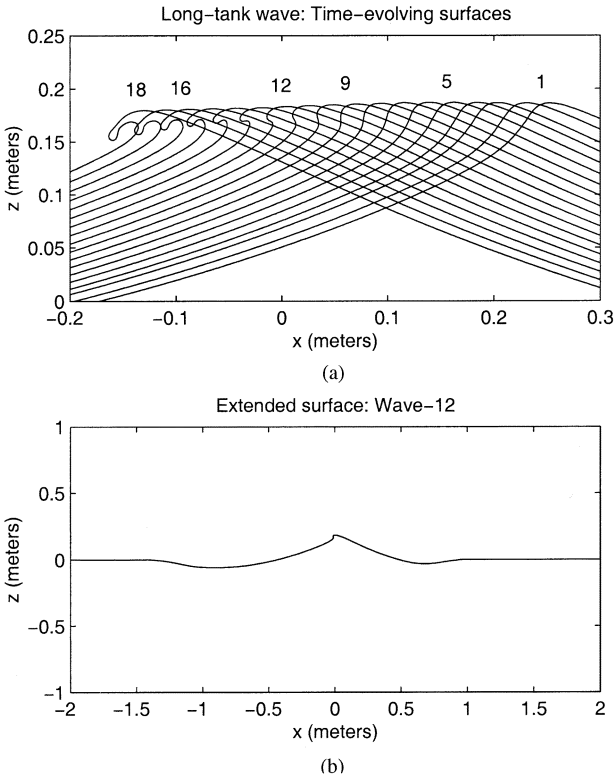


Fig. 1. Ocean-breaking waves from the "longtank" simulation.

In this paper, radar images of breaking waves computed from numerical scattering model data are investigated. High-resolution radar images formed from back-projection tomography of frequency- and angle-swept backscatter data are considered as polarization and surface profiles are varied. Breaking-wave profiles are obtained from the "longtank" numerical hydrodynamic simulation [13] applied in several previous studies [3]–[5]. Surface-scattering calculations are performed using the "generalized forward–backward (FB) method," which remains effective even with the multivalued surface profiles obtained as wave breaking occurs [14]. Time-domain and radar image results are described to illustrate the important scattering mechanisms. A ray-tracing analysis based on a "four-path" multipath model [15], [16] is applied to predict secondary scattering sources observed in the radar images. Small-scale surface roughness effects are also discussed.

## II. Scattering Geometry and Numerical Model

One-dimensional simulated sea waves obtained from the "longtank" numerical model of the University of California, Santa Barbara [13] are considered in this paper. Fig. 1(a) de-

picts profiles of the time-evolving longtank waves from [13, Fig. 1]; plotted are a total of 18 wave profiles that describe steepening waves through fully developed breaking waves. A more detailed description of these profiles is provided in [3]; note that no small-scale surface roughness is contained in these profiles. Being coarsely and unequally sampled, the original surface points are interpolated so that a sufficient number of unknowns per wavelength throughout the profile can be obtained for numerical electromagnetic simulations. In addition, in the case of near-grazing incidence that results in large spot sizes for a tapered incident wave, the original surfaces are horizontally extended to avoid scattering contributions from surface edges, as illustrated in Fig. 1(b). The inclusion of an extended flat surface is also important if multipath reflection from points away from the breaking region becomes significant.

The medium is assumed to be described by an impedance boundary condition with a relative permittivity of $(39.7+i40.2)$ to approximate the high conductivity sea water at X-band. The surface length in this study is chosen to be $L = 8.78$ m with 4096 surface points. A phase-corrected tapered beam with spot size $g = L/5$ is used to confine the incident field to this length [17]. It should be noted that in the scattering calculations all surface profiles are shifted so that the peak point of each profile is located at the center of the spot. The tapering parameter given above is sufficient to provide accurate surface scattering calculations up to the maximum 80° incident angle considered in this paper [18].

An important part of the longtank wave is the breaking portion of the surface, where the surface profile becomes multivalued, as shown in Fig. 1. Since standard analytical formulas for rough-surface backscattering do not apply to this type of surface, only numerical results are considered in this study. An improved iterative method of moments (MoM) solution is employed to treat surfaces with multivalued profiles, since some conventional iterative methods may have convergence problem in these cases. The generalized forward–backward (GFB) method is based on combination of a direct matrix calculation for the region containing obstacles (ship targets or large breaking waves) with the FB iterative algorithm for the rest of the area [14]. To improve the efficiency of the calculations, a novel spectral acceleration (NSA) technique for "weak" interaction region in the forward–backward iterative procedure is also applied so that radar images can be formed in a reasonable computational time [10], [11]. In the backscatter simulation, the number of points in the direct MoM region is fixed to 120 surface points (about 0.2 m) for all surface profiles. The size of the strong region for the NSA algorithm was set to 0.5 m and was found in tests to provide accurate backscatter results for all cases. For horizontal (HH) polarization, an electric field integral equation is used. In most cases, six or seven iterations are required to obtain a backscatter result. For vertical (VV) polarization, a smaller number of iterations is required (two or three iterations for all cases) by using a magnetic field integral equation. For a large surface with a relatively small direct MoM region, the resulting computation count and memory requirement reduce to $O(N)$, where $N$ is the number of surface unknowns.

A two-dimensional (2-D) SAR image of a deterministic surface is constructed from a set of frequency- and angular-swept complex backscattered field data. This corresponds to a "spotlight" SAR image in which the incident beam is oriented to illuminate a fixed surface area. Note the 2-D surface geometry does not allow realistic "side-looking" image formation: here the range direction lies in the same plane as the circular arc of the "platform" path. Back-projection tomography using an inverse Fourier transform is employed to generate the images [19]. For normal incidence, the down- and cross-range directions coincide with the $-z$ and $+x$ axes as shown in Fig. 1, respectively (i.e., the incident field approaches the surface from above). Down- and cross-range resolutions of the image can be determined by the frequency and angular bandwidths, respectively.

Backscatter data were collected over a 4-GHz frequency bandwidth (10–14 GHz) and a 20° angular bandwidth (60° to 80°) to allow 3.75-cm down-range and 3.65-cm cross-range resolutions in the image domain, respectively. The above image resolutions are reasonable in this problem to discern important scattering features. Frequency and angle steps are chosen (50 MHz and 0.4°, respectively) so that unambiguous ranges include possible secondary scattering sources in cases involving multiple scattering. A total of 4000 ($80\times50$) repeated numerical scattering model computations are needed to obtain an SAR image. With the GFB parameters mentioned above, the overall computation time on a 500-MHz CPU becomes approximately 100 h for HH polarization and about 50 h for VV polarization. This was reduced to 25 and 12 h, respectively, through the use of four processors. If necessary, an interpolation of far-zone backscattered fields or of surface-induced currents can be applied to improve frequency or angle sampling rates, resulting in reduced computation time. Interpolation issues are discussed in Section III. To obtain a high-resolution image with moderate side-lobe levels the Kaiser-Bessel window ($\beta = 2$) is applied to both frequency and angle data [20].

## III. Backscattering Results

### A. Time-Domain Responses

Time-domain results are obtained from frequency-swept (10–14 GHz) backscatter data at a fixed incident angle. Both HH and VV time-domain responses for waves 12 and 16 at 70° incident angle are presented to illustrate important scattering centers and polarization effects. As shown in Fig. 2, envelope time-domain results for wave-12 show three discernible peaks around the reference time ($t = 0$ ns), which is defined at the center of the axes ($(x, z) = (0, 0)$). Since there is little backscattering from the flat portion of the surface, and the breaking wave is located above the reference plane ($z = 0$), direct scattering from the breaking region is expected to occur at earlier times. The first peak near $t = -0.5$ ns, therefore, corresponds to the direct backscattering from the breaking region of the surface. The polarization ratio for direct backscattering (HH/VV) of wave-12 is about 20 dB, indicating a "superevent" type of behavior for the direct backscattering term. West [4], [21] employed a MoM solution combined with geometrical diffraction theory (MM/GTD) for the same wave profiles and observed similar

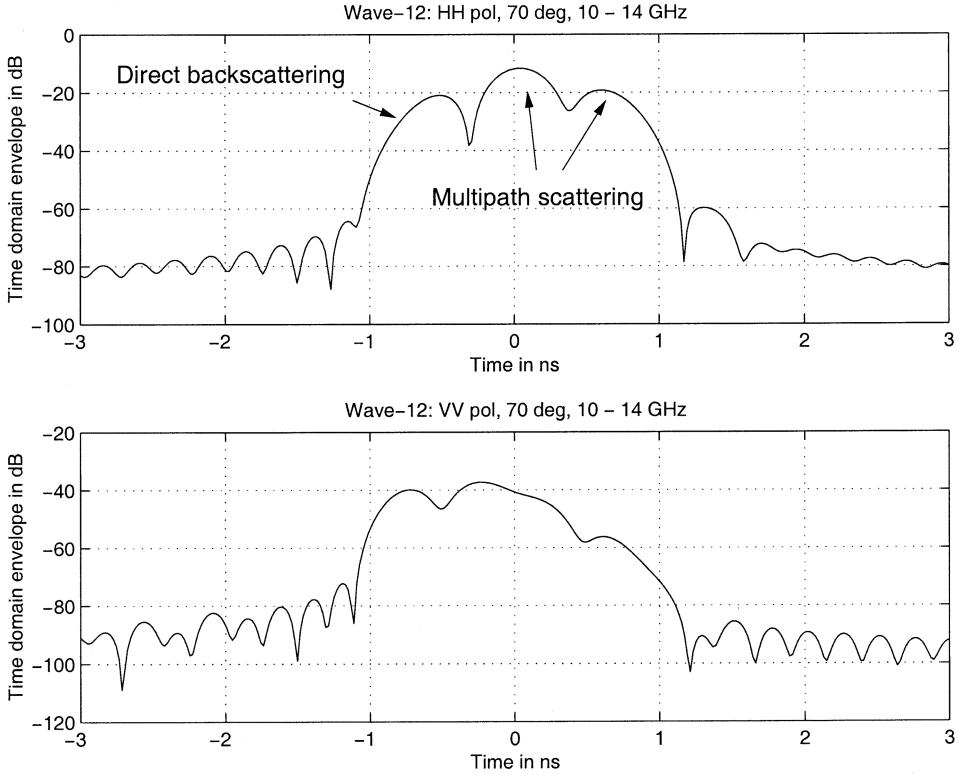


Fig. 2. Envelope time-domain response for wave-12: $f = 10$–$14$ GHz, $\delta f = 50$ MHz, $\theta_i = 70°$. (a) HH polarization; (b) VV polarization.

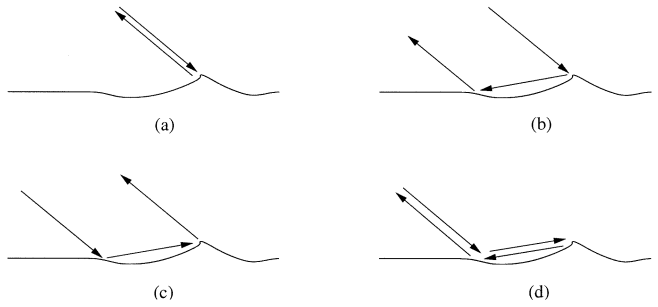


Fig. 3. Scattering mechanism of four-path model. (a) Path 1 (b). Path 2. (c) Path 3. (d) Path 4.

large HH/VV ratios from an isolated breaking region (without multipath scattering) at stages wave-9 through wave-18.

Compared to the first peak, the contribution of the peaks at later times is also significant and originates from time-delayed multipath scattering. To describe the secondary peaks, it is useful to incorporate a multipath scattering model to identify the nondirect scattering terms. Previous studies [5], [6] have shown that the "four-path" model can be used as a physical basis for multipath scattering phenomena. Johnson [15], [16] also employed this "four-path" model to examine the scattering from an object above a rough surface. The breaking portion of the surface can be treated as a target above a surface, and the four-path model can be effective to analyze the secondary scattering mechanisms. As shown in Fig. 3, the four-path model involves a standard backscattering path from the surface breaking points (path 1), a bistatic scatter from the breaking points preceded or followed by a reflection from the flat portion of the surface (paths 2 and 3) representing single-bounce processes, and finally, a bistatic scatter from the breaking points preceded and followed by a reflection from the flat portion of the surface (path 4) representing a double-bounce mechanism.

According to the multipath model, the second peak corresponds to the sum of paths 2 and 3, which are reciprocal paths that contribute to the peak coherently. Analysis of time delays for the single-bounce path shows an expected return around $t = 0$. For the case of wave-12, the level of multipath scattering by paths 2 and 3 is comparable (for VV polarization) to or even larger (for HH polarization) than the direct scattering peak, implying a strong bistatic contribution from the breaking points. Smaller levels of multipath returns for the VV case compared to the HH case can occur due to smaller bistatic scattering from the breaking region in VV polarization, or due to the reduced reflection coefficient in VV polarization for the single- and double-bounce paths off the front surface of the breaking wave. Although the pseudo-Brewster angle for VV polarization occurs beyond the maximum 80° incident angle considered here, differences between vertically and horizontally polarized reflection coefficients are still significant, as will be further discussed when examining radar images. Time domain returns from waves 1–18 (not plotted) show that, in the earlier stages of the waves, the multipath scattering effects are negligible, and direct backscattering from the crest region of the surface dominates the overall scattering process. As the surface evolves, the multipath scattering effects become more significant.

In Fig. 4, time-domain responses are plotted for wave-16. The VV return shows an increased direct backscatter return, while HH shows a direct backscatter return similar to wave-12. Multipath scattering effects are decreased as compared to wave-12 in both polarizations. Though strong multipath effects are ob-

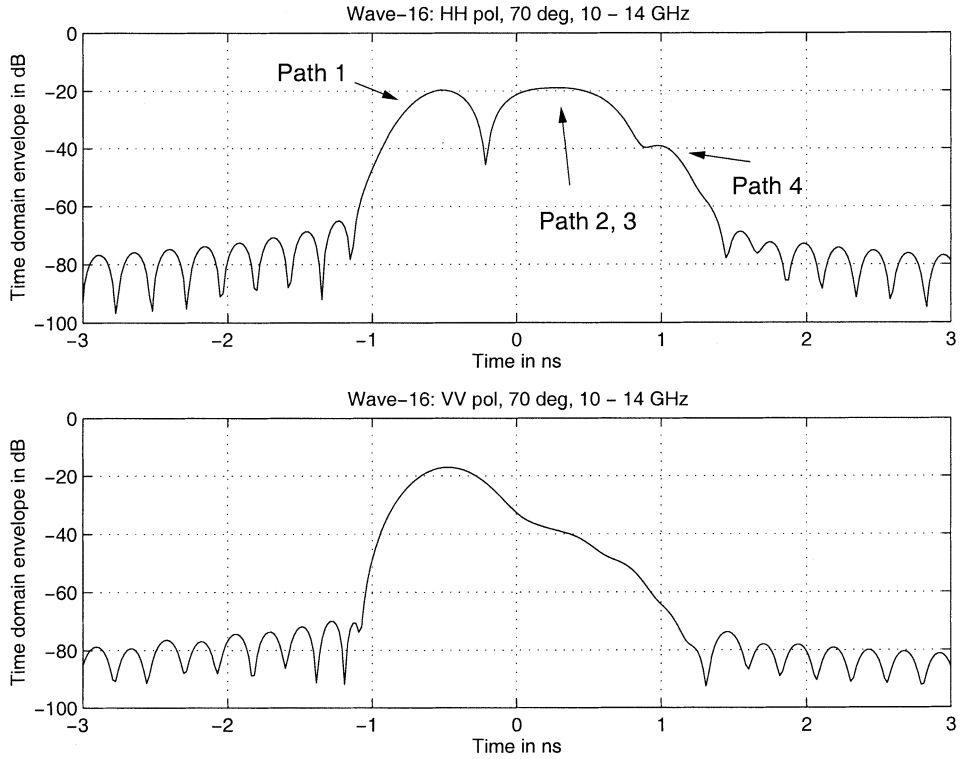


Fig. 4. Envelope time-domain response for wave-16: $f$ =10–14 GHz, $\delta f$ = 50 MHz, $\theta_i$ = 70°. (a) HH polarization; (b) VV polarization.

served for both waves, the dominant scattering mechanism that produces the large HH/VV ratio is the direct backscattering term and is due to the geometrical structure of the breaking region, as discussed in [21]. Radar images in Section III-B will further clarify scattering mechanisms observed in the time-domain results. The images are also used to confirm the surface points that are associated with multipath scattering contributions.

### *B. Two-Dimensional Radar Image Results*

In Fig. 5, HH and VV polarized radar images obtained from numerical results are plotted for wave-12. The surface profile is also overlaid to verify the image source locations. As shown in the figure, strong backscatter returns for single scattering are observed from the breaking points for both polarizations. In addition to the single-scattering returns that appear on the surface profile, multiple-scattering effects due to interaction between breaking points and the profile front surface are observed below the surface.

A ray-tracing analysis based on the four-path model can be used to estimate locations and associated surface points for secondary scattering images. In a previous study [12], for all surface point pairs, a ray-tracing analysis was conducted to verify locations of multiple-scattering images. For breaking waves, the analysis is performed between breaking points and all other surface points. First, as illustrated in Fig. 6, we draw rays that connect incident and scattering rays to represent the single- and double-bounce mechanisms, respectively. Next, by calculating the time-delay of each ray, the locations of additional images can be obtained for the two different scattering mechanisms. This process is repeated for all surface points outside the breaking region. As a final step, the corresponding time-delayed points are placed along the down-range from the center of the two

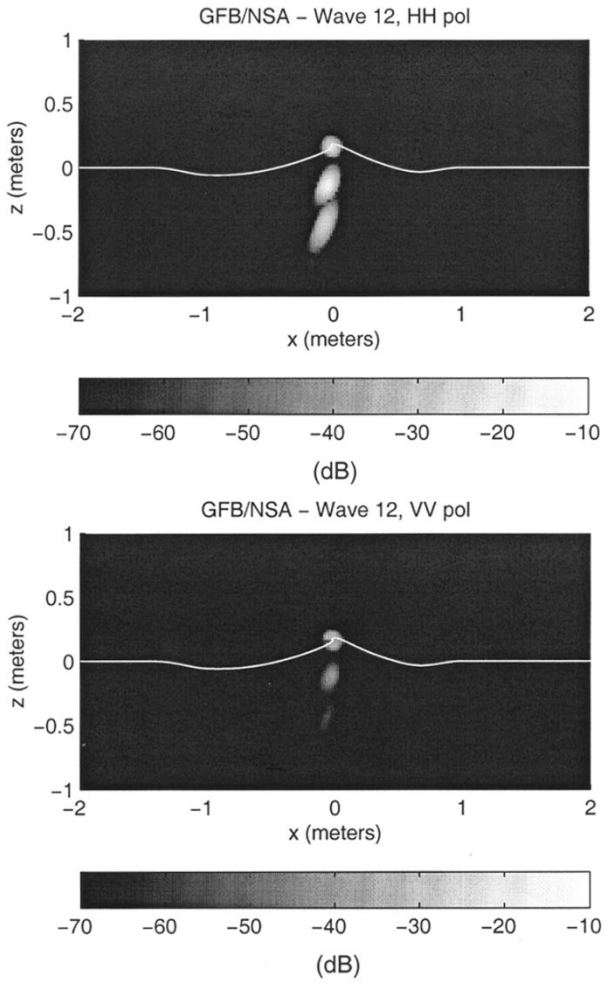


Fig. 5. Two-dimensional backscattering radar images of wave-12: $f$ =10–14 GHz, $\delta f$ = 50 MHz, $\theta_i$ = 60° to 80°, and $\delta\theta$ = 0.4°.

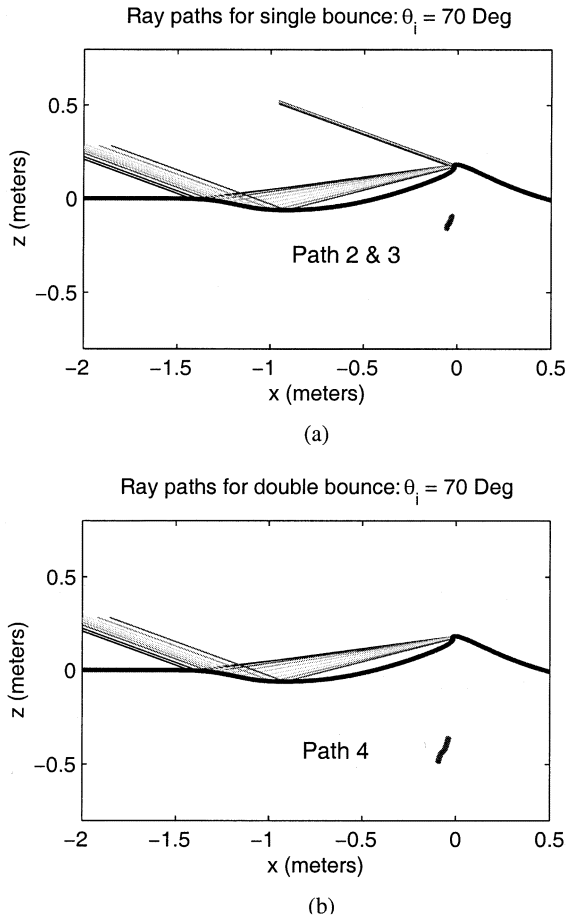


Fig. 6. "Four-path" ray-tracing prediction for the location of time-delayed multipath images at 70° incident angle.

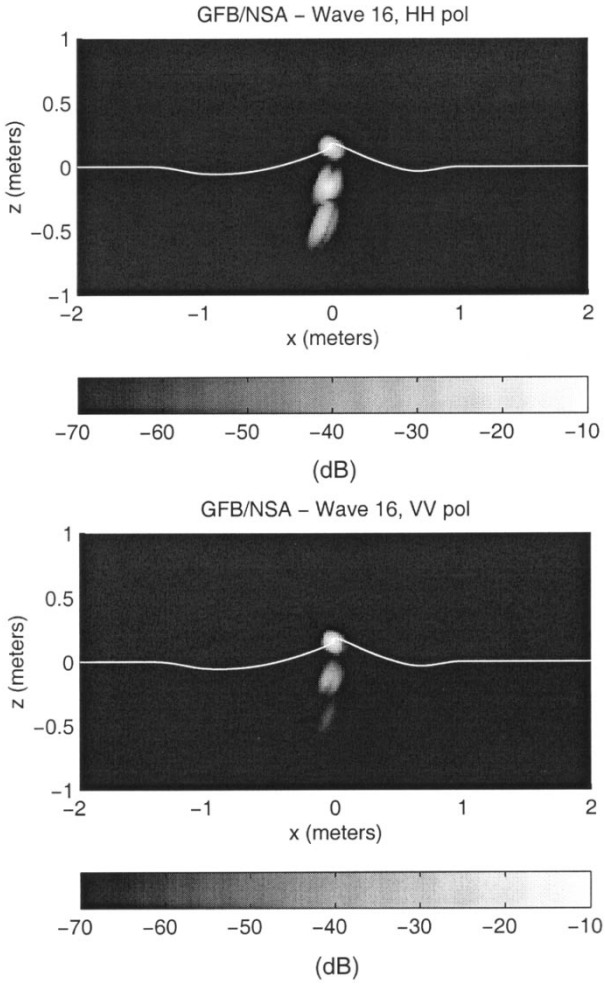


Fig. 7. Two-dimensional backscattering radar images of wave-16: $f$ =10–14 GHz, $\delta f$ = 50 MHz, $\theta_i$ = 60° to 80°, and $\delta\theta$ = 0.4°.

points (a specular reflection point and a breaking point) for the single-bounce mechanism, and from the specular reflection points for the double-bounce mechanism. Overlaid on the image domain, the predicted points match the time-delayed images very well, justifying the basic ideas of the four-path model.

As observed in Fig. 5, significant polarization differences are observed for wave-12 images. The maximum image levels are −14.2 dB for HH polarization and −36.2 dB for VV polarization. The strongest image points for HH polarization come from the strong single-bounce term, which is 6.8 dB higher in amplitude than the direct single-scattering term (−21.0 dB). The double-bounce term (−24.1 dB) is also comparable to the direct backscattering term. The VV image shows a dominant direct backscattering image level (−36.1 dB) and relatively weak multipath scattering contributions (−45.0 dB and −61.1 dB for single- and double-bounce terms, respectively). Similar polarization behaviors were observed for time-domain results in Section III-A. For VV polarization, some discrepancies between time-domain and image results are observed. Time-domain results in Fig. 2 showed similar levels between direct backscattering and the single-bounce scattering. However, image results show some differences between these two scattering terms. This may be due to the coherent averaging over the wide range of incident angles in the image formation.

For wave-16, as shown in Fig. 7, the maximum scattering occurs from the single-scattering returns for both polarizations (−19.4 dB for HH and −17.4 dB for VV). The VV image shows greatly increased direct scattering returns compared to wave-12, while HH returns are only slightly increased. For HH polarization, the single- and double-bounce terms are 2.2 dB and 8.4 dB lower than the direct backscattering, respectively, while VV polarization produces 21.2-dB and 40.2-dB lower returns in single- and double-bounce terms.

In Fig. 8, plots are shown of the maximum image intensity and the polarization ratios of each scattering mechanism for wave-1 through wave-16. As shown in Fig. 8(a) and (b), the direct backscattering level ranges from −27.3 dB (wave-2) to −13.94 dB (wave-8) for HH and from −36.1 dB (wave-12) to −14.2 dB (wave-8) for VV. In the earlier stages before breaking, the single- and double-bounce mechanisms are much lower than direct backscattering. While the VV image intensity produces multipath scattering terms that never exceed direct backscattering, the HH image yields larger single-bounce returns than direct scattering for waves 10–13. For the wave-13 case, all three HH scattering terms yield similar amplitudes within a 4-dB range. An interesting feature in the wave-14 HH image is that the double-scattering term is slightly higher than the single-bounce term by 2.4 dB. The ratio between the direct and single-bounce scattering mechanisms is plotted in Fig. 8(c). For all cases, VV shows an approximately 10-dB greater ratio between scattering processes than HH. Reflection

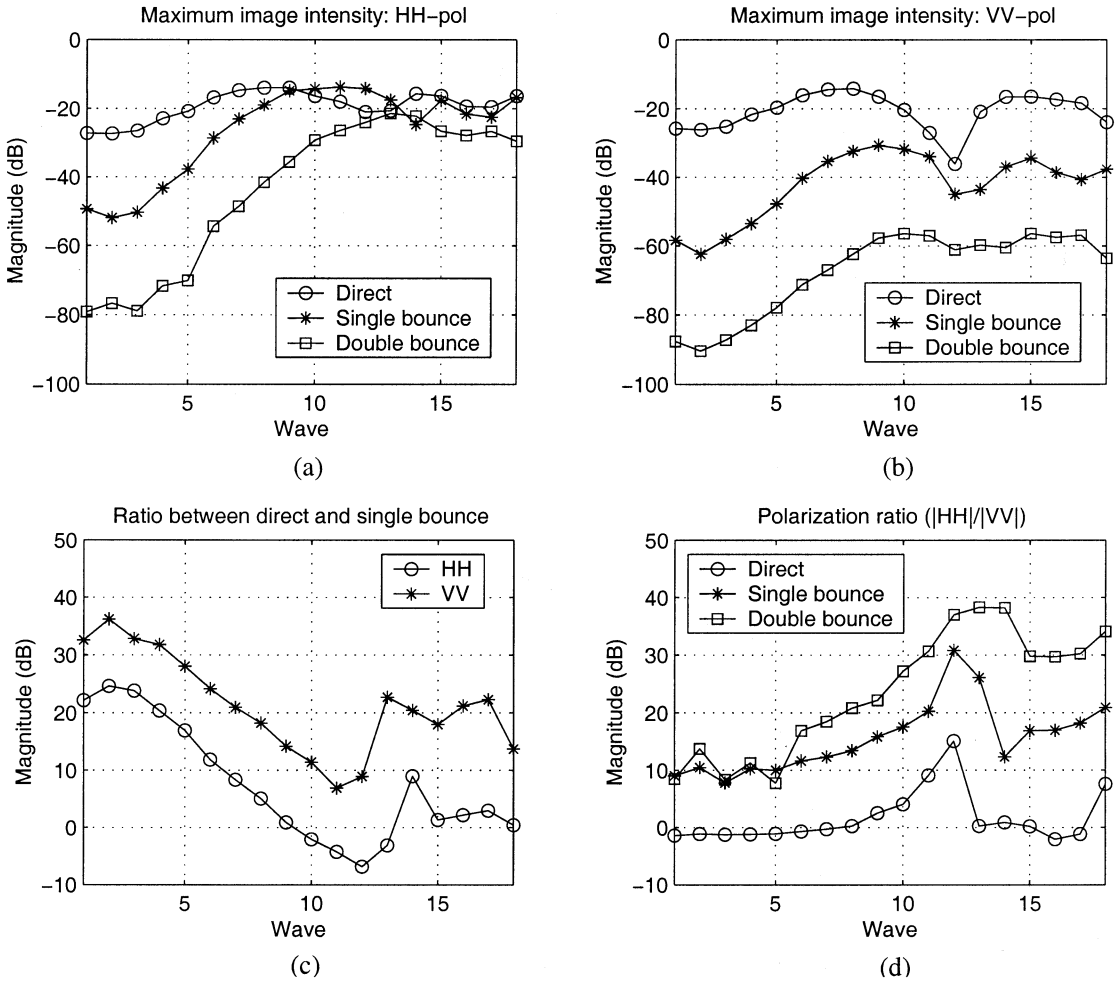


Fig. 8. (a) Maximum HH image domain amplitudes. (b) Maximum VV image domain amplitudes. (c) Image domain ratio of direct and single-bounce mechanisms. (d) Polarization ratios of scattering mechanisms.

coefficients for reflection from a flat surface show a ratio between polarizations ranging from 3.2–12.1 dB (average 6.7 dB) over 60° to 80° incident angles, so that some of this difference can be interpreted as due to the Fresnel reflection coefficient. The remainder is thought to be due to the polarization differences in breaking region diffraction effects. Fig. 8(d) shows the polarization ratio for each scattering process. For all cases except wave-9 to wave-12, the direct scattering shows a similar backscatter level for both polarizations. For wave-9 to wave-12, the HH/VV ratio increases up to 15 dB. For the single- and double-bounce mechanisms, HH/VV ratios are greater than 10 dB for most cases.

### *C. Breaking Wave With Small-Scale Roughness*

As a more realistic case, surface roughness is introduced on the flat portion of the breaking wave. The surface roughness outside the breaking region is added through a Pierson–Moskowitz (P–M) power-law spectrum to approximate a rough-sea surface. Recently, surface roughness effects on breaking-wave scattering using a P–M spectrum have been addressed. Zhao *et al.* [22] employed a model-based approach to calculate coherent and incoherent radar cross sections using Monte Carlo simulation over many rough-surface realizations. In this section, radar images are constructed for particular profiles to observe the effects of surface roughness for both polarizations. Due to the strong scattering contributions from the small-scale roughness that increase the range of scattering sources in the image domain, a smaller frequency step size (25 MHz) in image formation is needed. In this paper, a simple interpolation algorithm for surface currents versus frequency has been applied to reduce the overall computation time to obtain an alias-free radar image. To improve the accuracy of the interpolation, surface currents are first divided by the incident field phase factor (a function of frequency, angle, and position) because this factor produces rapid variations in frequency particularly near surface edges. The interpolation is then performed on the more slowly varying "phase-extracted" currents and the incident field phase factor included again after the interpolation. Tests for a subset of observation angles showed surface currents interpolated to a 25-MHz step from a 50-MHz step original data to be in good agreement with exact 25-MHz step results. Note that this process does not require that the surface current variation versus frequency be entirely determined by the incident field phase factor, but rather simply attempts to improve the accuracy of the interpolated values obtained.

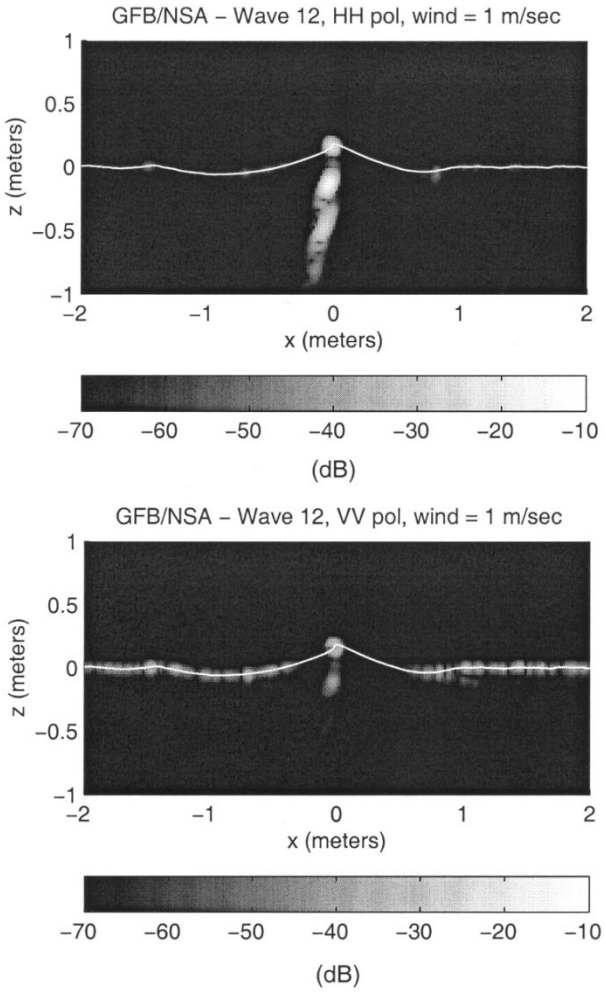


Fig. 9. Two-dimensional backscattering radar images of wave-12 with roughness (wind = 1 m/s): $f$ =10–14 GHz, $\delta f$ = 50 MHz, $\theta_i$ = 60° to 80°, and $\delta\theta$ = 0.4°. Frequency step in the VV image is 25 MHz (interpolated from 50-MHz step).

Fig. 9 shows radar images of wave-12 with surface roughness generated by a 1-m/s wind speed. As shown in the figure, direct backscattering for HH polarization from the rough-surface region is negligible compared to the direct scattering from the breaking region. The overall backscattering level is not sensitive to the surface roughness for HH case. However, for the VV case, the single-scattering returns from the rough surface are much higher than the HH case and are even comparable to the direct backscattering term. This is due to the strong Bragg scattering returns from the small-scale rough surface. Due to the roughness on the surface, it is not appropriate to apply the ray-tracing algorithm to predict the multipath scattering returns. However, we can observe how the surface roughness can affect the multipath scattering mechanisms in the image domain. As compared to the flat surface case, the multipath scattering spots appear as blurred images due to diffraction effects of the surface roughness.

## IV. Conclusion

Backscatter responses of breaking waves have been studied through numerical calculations. Time-domain results and radar images showed the importance of the geometrical shape of the breaking region and multipath scattering effects associated with single- and double-bounce scattering terms. Due to strong bistatic contributions from the breaking region for some wave profiles (after wave-9), not only direct scattering from the breaking part of the wave affects the scattering, but also the multipath returns contribute to the overall radar cross sections. Wave-12 shows the largest HH/VV ratio (about 20 dB when compared between the single-bounce term in HH and direct backscattering term in VV) due to a null behavior of VV direct backscattering from the breaking region and strong multipath returns for HH.

Ray-tracing analysis confirmed the origin of additional radar image points observed below the surface boundary, revealing that the four-path model can be used as a basic model to predict the main scattering mechanisms from breaking waves. Image studies of small-scale roughness effects have also been conducted, and they showed the effect of the roughness on HH and VV images and on multipath scattering terms. To reduce the overall computation time, a simple interpolation algorithm over surface currents was applied, and aliasing effects observed in radar images formed by undersampled frequency data were successfully removed without degrading the main scattering features. Though computational requirements make it difficult to obtain finer resolution images, results show that image studies can improve the understanding of basic scattering mechanisms involved in scattering from breaking waves.

## References

[1] L. B. Wetzel, "Sea clutter," in *Radar Handbook*, 2nd ed, M. I. Skolnik, Ed. New York: McGraw-Hill, 1990, ch. 13.

[2] ——, "Electromagnetic scattering from the sea at low grazing angles," in *Surface Waves and Fluxes*, G. L. Geernaert and W. L. Plant, Eds. Dordrecht, The Netherlands: Kluwer, 1990, vol. II, pp. 109–171.

[3] D. Holliday, L. L. DeRaad Jr, and G. J. St-Cyr, "Sea-spike backscatter from a steepening wave," *IEEE Trans. Antennas Propagat.*, vol. 46, pp. 108–113, Jan. 1998.

[4] J. C. West, J. M. Sturm, and S.-J. Ja, "Low-grazing scattering from breaking water waves using an impedance boundary MM/GTD approach," *IEEE Trans. Antennas Propagat.*, vol. 46, pp. 93–100, Jan. 1998.

[5] J. C. West, "Ray analysis of low-grazing scattering from a breaking water wave," *IEEE Trans. Geosci. Remote Sensing*, vol. 37, pp. 2725–2727, Nov. 1999.

[6] D. B. Trizna, "A model for Brewster angle effects on sea surface illumination for sea scatter studies," *IEEE Trans. Geosci. Remote Sensing*, vol. 35, pp. 1232–1244, Sept. 1997.

[7] S. E. Shih, K. H. Ding, Y. Zhang, and J. A. Kong, "Subsurface detection based on enhanced SAR signatures using angular correlation function," in *Proc. IGARSS*, Seattle, WA, 1998, pp. 530–532.

[8] G. Zhang and L. Tsang, "Application of angular correlation function of clutter scattering and correlation imaging in target detection," *IEEE Trans. Geosci. Remote Sensing*, vol. 36, pp. 1485–1493, Sept. 1998.

[9] H. Kim and J. T. Johnson, "Radar images of rough surface scattering: Comparison of numerical and analytical models," *IEEE Trans. Antennas Propagat.*, vol. 50, pp. 94–100, Feb. 2002.

[10] H.-T. Chou and J. T. Johnson, "A novel acceleration algorithm for the computation of scattering from rough surfaces with the forward-backward method," *Radio Sci.*, vol. 33, pp. 1277–1287, 1998.

[11] D. Torrungrueng, J. T. Johnson, and H. T. Chou, "Some issues related to the novel spectral acceleration method for the fast computation of radiation/scattering from one dimensional extremely large scale quasiplanar structures," *Radio Sci.*, vol. 37, pp. 3(1)–3(20), 2002.

[12] H. Kim and J. T. Johnson, "Radar image studies of an ocean-like surface," *Microwave Opt. Technol. Lett.*, vol. 30, pp. 381–384, Sept. 2001.

[13] P. Wang, Y. Yao, and M. P. Tulin, "An efficient numerical tank for nonlinear water waves, bases on the multi-subdomain approach with B.E.M.," *Int. J. Numer. Meth. Fluids*, vol. 20, pp. 1315–1336, 1995.
[14] M. R. Pino, L. Landesa, J. L. Rodriguez, F. Obelleiro, and R. J. Burkholder, "The generalized forward-backward method for analyzing the scattering from targets on ocean-like rough surfaces," *IEEE Trans. Antennas Propagat.*, vol. 47, pp. 961–969, June 1999.
[15] J. T. Johnson, "A study of the four-path model for scattering from an object above a halfspace," *Microwave Optic. Technol. Lett.*, vol. 30, pp. 130–134, 2001.
[16] ——, "A numerical study of scattering from an object above a rough surface," *IEEE Trans. Antennas Propagat.*, 2002, to be published.
[17] E. I. Thorsos, "The validity of the Kirchhoff approximation for rough surface scattering using a Gaussian roughness spectrum," *J. Acoust. Soc. Amer.*, vol. 83, pp. 78–92.
[18] D. A. Kapp, "A new method to calculate wave scattering from rough surfaces at low grazing angles," Ph.D. dissertation, Virginia Polytechnic Inst. State Univ., Blacksburg, 1995.
[19] D. L. Mensa, *High Resolution Radar Cross Section Imaging*. Norwood, MA: Artech House, 1991.
[20] F. J. Harris, "On the use of windows for harmonic analysis with the discrete Fourier transform," *Proc. IEEE*, vol. 66, pp. 51–83, 1978.
[21] J. C. West, "LGA sea-spike backscattering from plunging breaker crests," *IEEE Trans. Geosci. Remote Sensing*, vol. 40, pp. 523–526, Feb. 2002.
[22] Z. Zhao and J. C. West, "Modeling of multipath scattering from breaking water waves with rough faces," in *Proc. IGARSS*, Sydney, Australia, 2001.

**Hyunjun Kim** (S'02) received the B.E. degree in electronics engineering from Chung-Ang University, Seoul, Korea, in 1991, and the M.S. and Ph.D. degrees in electrical engineering from The Ohio State University, Columbus, in 1998 and 2002, respectively.

He is currently a Senior Package Design Engineer with Intel Corporation, Chandler, AZ, where he works on research and development in the areas of signal integrity, I/O interconnect, and EMI. From 1995 to 1996, he was a Research Staff Member for the Korea Telecom R&D Group, Seoul, Korea, where he was involved in measurement and analysis of ATM network testbeds. His research interest include computational electromagnetics, microwave remote sensing, and electromagnetic modeling of high-speed electronic packaging systems.

**Joel T. Johnson** (M'96) received the B.S. degree in electrical engineering from the Georgia Institute of Technology, Atlanta, in 1991 and the S.M. and Ph.D. degrees from the Massachusetts Institute of Technology, Cambridge, in 1993 and 1996, respectively.

He is currently an Associate Professor in the Department of Electrical Engineering and ElectroScience Laboratory, The Ohio State University, Columbus. His research interests are in the areas of microwave remote sensing, propagation, and electromagnetic wave theory.

Dr. Johnson is a Member of Commissions B and F of the International Union of Radio Science (URSI), and he is a member of Tau Beta Pi, Eta Kappa Nu, and Phi Kappa Phi. He received the 1993 Best Paper Award from the IEEE Geoscience and Remote Sensing Society, and he was named an Office of Naval Research Young Investigator, National Science Foundation Career awardee, and PECASE Award recipient in 1997. In 2002, he was recognized by the U.S. National Committee of URSI as a Booker Fellow.